36th European Rotorcraft Forum - Paris, France, 7-9 September 2010

Paper 096

Simulation of a Complete Helicopter: a CFD Approach to the Study of Interference Effects

M.Biava[1], L.Vigevano[2]

[1] AgustaWestland-Politecnico Advanced Rotorcraft Center (AWPARC), Milano, Italy. biava@aero.polimi.it

[2] Dipartimento di Ingegneria Aerospaziale, Politecnico di Milano, Italy. luigi.vigevano@polimi.it

Abstract

Simulations performed with the RANS solver ROSITA of an isolated rotor, an isolated fuselage and a full helicopter configuration, featuring both main and tail rotors, are compared to analyze the interference effects between the rotor wakes and the fixed components of the fuselage and the influence of the fuselage on the rotor loads. At the same time the experimental data gathered from the GOAHEAD database are compared with computations, to assess the viability of such CFD tool for aerodynamic interference studies.

1 Introduction

The modern helicopter industry requires design tools which are capable of predicting accurately and efficiently the complex aerodynamic flow field generated by the helicopter main rotor, and also to correctly capture the interference effects between the rotor wakes and the different fuselage parts and control surfaces. A satisfactory representation of rotor-fuselage aerodynamic interactions is critical to predict rotorcraft performances. The unsteady loads due to the rotor wake impact on the fuselage and on the empennage may produce vibrations and also modify the helicopter controls under certain flight conditions. The main rotor inflow may also been altered in the presence of the fuselage, especially for the compact designs which are developed nowadays.

A classification of the categories of aerodynamic interactions was introduced in a seminal paper by Sheridan and Smith [1]. Since then several contributions appeared in the literature, both experimental and numerical. Experiments with a simple teetering main rotor mounted over cylindrical fuselage shape have been carried out at Georgia Tech. [2], [3], while more realistic fuselage shapes, although without control surfaces and tail rotor, were considered at University of Maryland [4], [5] and for the rotor-body interaction (ROBIN) test case of NASA [6], [7]. These three experimental data sets – due to their geometrical simplification and to the lack of experimental measurements over realistic configurations – have been extensively used for the validation of several numerical approaches to the interference problem, see for instance [8], [9].

Present CFD tools are able to simulate the turbulent flow past a complete helicopter [10], [11], even considering fluid-structure coupling [12], [13]. The lack of suitable experimental data for realistic helicopter geometries prevented, however, their thorough validation in the past. To address this need, the European Project GOAHEAD has created an extensive experimental data base for a complete helicopter configuration [14] which will be used as a benchmark for CFD methods validation [15], [16].

In the present paper, some experimental data from the GOAHEAD database are compared with computations, performed with the CFD code ROSITA (ROtorcraft Software ITAly) [17], [18], based on the solution of the Reynolds Averaged Navier–Stokes (RANS) equations coupled with the one-equation turbulence model of Spalart–Allmaras. By comparing simulations of the isolated fuselage, of the isolated rotor and of the full helicopter, the interference effects between the main and tail rotors and the fixed components of the fuselage shall be analyzed.

2 Description of the CFD code

The ROSITA flow solver [19] numerically integrates the RANS equations, coupled with the one-equation turbulence model of Spalart–Allmaras, in overset systems of moving multi-block grids. The equations are discretized in space by means of a cell-centred finite-volume implementation of the Roe's scheme. Second order accuracy is obtained through the use of MUSCL extrapolation supplemented with a modified version of the Van Albada limiter introduced by Venkatakrishnan [20]. The viscous terms are computed by the application of the Gauss theorem and using a cell-centred discretization scheme. Time advancement is carried out with a dual-time formulation, employing a 2^{nd} order backward differentiation formula to approximate the time derivative and a fully unfactored implicit scheme in pseudo-time. The generalized conjugate gradient (GCG), in conjunction with a block incomplete lower-upper preconditioner, is used to solve the resulting linear system.

The connectivity between the (possibly moving) component grids is computed by means of the Chimera technique. The approach adopted in ROSITA is derived from that originally proposed by Chesshire and Henshaw [21], with modifications to further improve robustness and performance. For integration of the aerodynamic forces on overlapping surface grids (figure 1), the so-called "zipper-grid" technique of Chan and Buning [22] is used. It consists in eliminating the overlapped surface cells and in filling the created gap with triangles; the integration is then performed on the resulting hybrid mesh.

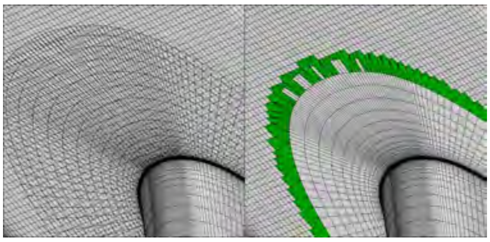

Figure 1: Overlapped surface grids (left) and hybrid surface mesh with zipper grid (right).

3 Numerical simulation

The numerical simulation of the GOAHEAD cruise test case has been performed on a computational mesh composed of 10 structured multi-block grids, for a total of 126 blocks and 27M cells (see figure 2). The grid for the strut, rotor head, main rotor blades and tail rotor blades were provided by DLR, but they were slightly modified in terms of node distribution in order to accommodate the strict requirements imposed by the ROSITA implementation of the Chimera algorithm. The background and fuselage grids were instead designed independently by the authors starting from the CAD of the scanned helicopter model.

Grid	No. Blocks	No. of Nodes ($\times 10^6$)
Fuselage	79	17.4
Main rotor blade ($\times 4$)	4	1.0
Tail rotor blade ($\times 2$)	6	0.5
Rotor hub	9	2.0
Strut	4	1.3
Wind tunnel	6	1.3
Total	126	27.0

Table 1: Computational mesh details.

The wind tunnel walls have been modelled with inviscid boundary conditions, whereas the fuselage, the strut, the main rotor and the tail rotor where modelled through no-slip boundary conditions. The time-accurate simulation was started from an undisturbed free stream condition (*i.e.* impulsive start) and three main rotor revolutions have been performed using a constant azimuthal step size $\Delta\Psi=1^\circ$. The number of pseudo-iterations for each azimuthal step was equal to 40, with CFL=7.0 for the mean flow and CFL=1.0 for the Spalart–Allmaras equation.

Both the main and tail rotor blades have been considered rigid, and their motion has been accounted for in the numerical model by means of the Chimera technique. The blade control angles were assumed equal to the ones measured during the wind tunnel test.

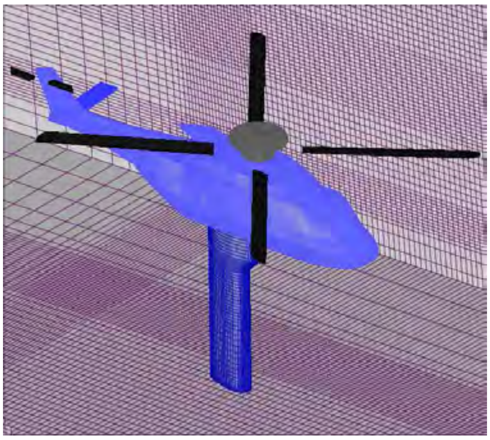

Figure 2: Surface grid on the model and wind tunnel walls.

4 Discussion of results

Computed results for the Isolated Rotor (IR), the Isolated Fuselage (IF) and the Complete Helicopter (CH) configurations will be compared to assess the interference effects. We will analyze separately the effect of the main and tail rotors on the fuselage loads and the flow field, and the effect of the fuselage on the rotor loads. At the same time, the CH numerical simulations will be assessed against the experimental results of the GOAHEAD database.

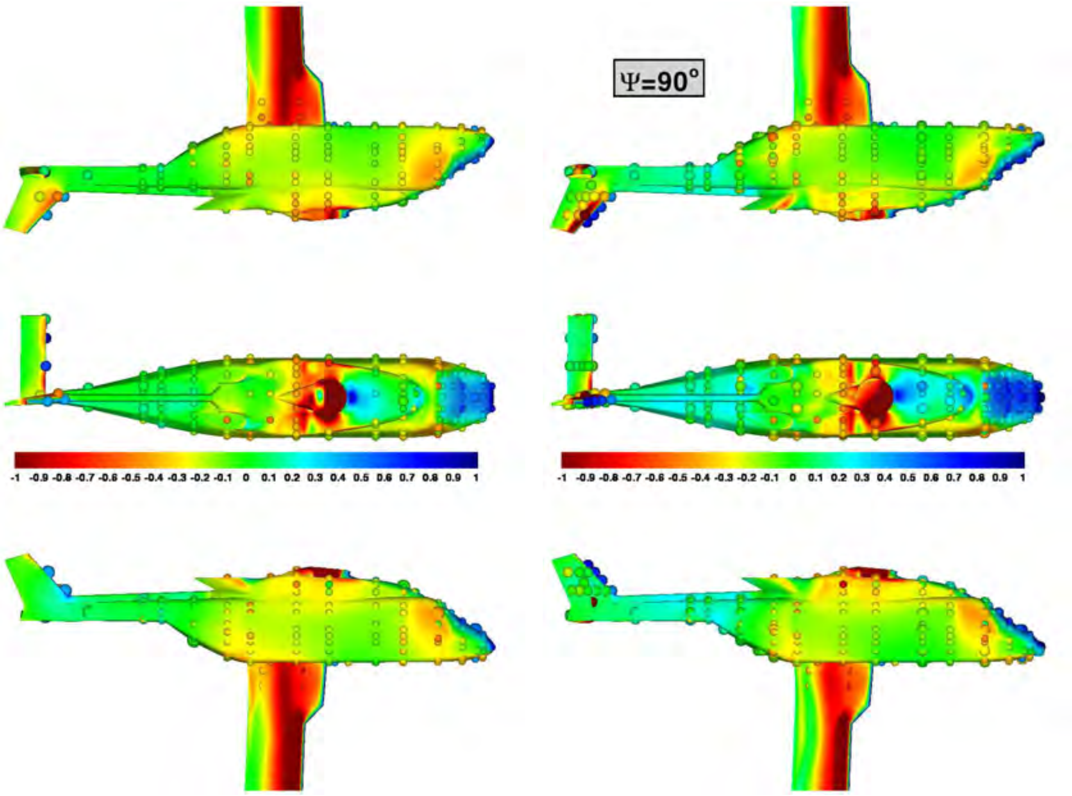

(a) Isolated Fuselage

(b) Complete helicopter at $\psi = 90^o$

Figure 3: Effect of main rotor on fuselage pressure distribution

4.1 Rotor on fuselage interactions

A general view of the pressure distribution on the fuselage surface is shown in figure 3. The dots on the fuselage skin refer to the experimental values of the pressure coefficient, gathered with both steady and unsteady pressure transducers. The overall agreement with the experimental data is reasonable. The CH configuration (figure 3(b)) is shown for the azimuth $\psi = 90^o$ where – for the present 4-bladed rotor – two blades are located over the fuselage in longitudinal direction and the interference is maximized. The influence of the blade passage can be seen as an increased pressure over the nose of the aircraft and over the right and top sides of the tail boom. Differences between IF and CH are reduced at other azimuthal angles.

The location of the unsteady pressure sensors is reported in figure 4. The time history of pressure at selected sensors is shown in figures 5, 7 and 11. Each figure is divided in two parts: part (a) shows the comparison between IF (steady value) and CH computed results, while part (b) shows the comparison of CH computations with experiments. In addition, the Fourier transforms of the measured and calculated CH results are shown in figures 6, 8 and 12 to better analyze the unsteady effects.

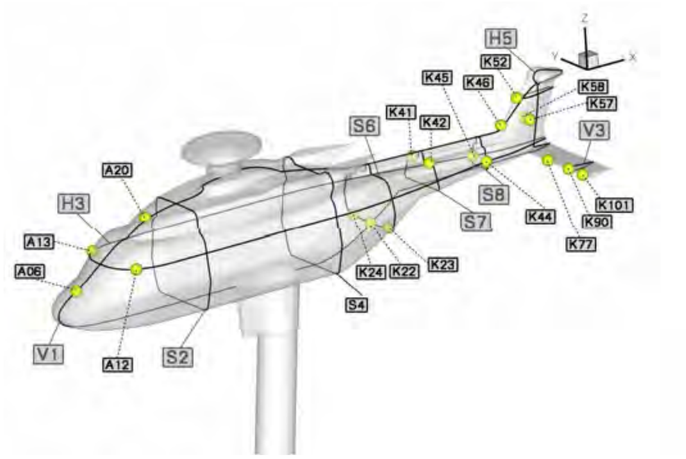

Figure 4: Location of the pressure sensors

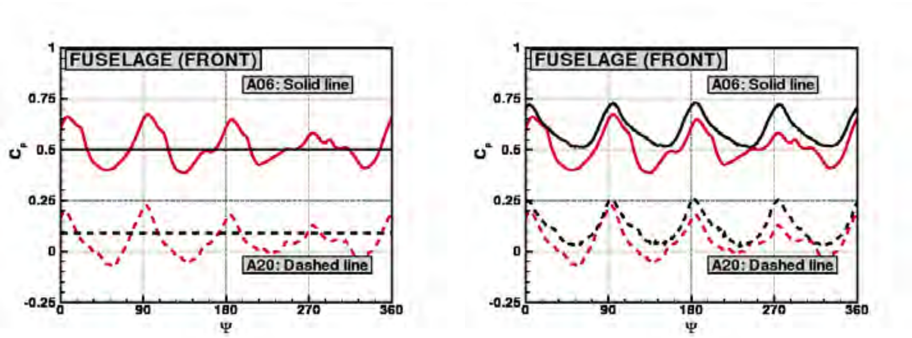

(a) Isol. Fuselage (black) vs Helicopter (red) (b) Comparison with experiments (black)

Figure 5: Effect of main rotor on fuselage pressure sensors A06-A20

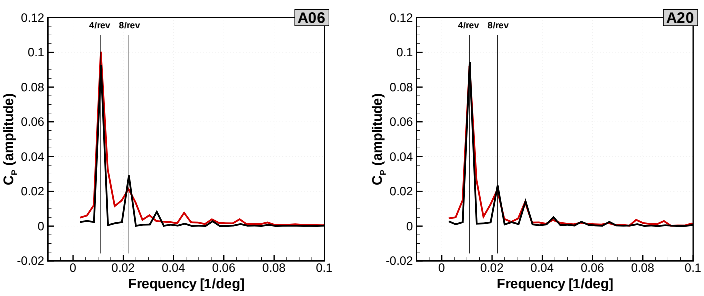

(a) A06 (b) A20

Figure 6: FFT of pressure signal for sensors A06-A20: experiments (black) and computations (red)

Sensors A06 and A20 (figure 5) refer to the aircraft front centerline (see figure 4). It is easy to notice the 4/rev oscillation of the CH results due to the blade passage, well confirmed by the experiments. The fourth blade signature is slightly less evident in the numerical results, suggesting that the three revolutions calculations are still not completely converged to a fully periodic solution. Comparison of the numerical and experimental data in the frequency domain (figure 6) confirms an excellent agreement and shows the occurrence of a 8/rev contribution. The averaged value of the pressure oscillations correlates quite well with the IF results, demonstrating that in the front part of the aircraft the interference effects are localized and mainly due to the blade passage. The pressure time history recorded by the two sensor located in the upper part of the tail boom, K41 (right) and K42 (left), shows again a dominant 4/rev oscillation frequency (see figure 7). The correlation of the averaged CH result with the IF value is less good than for the front part, indicating that the main rotor downwash deeply influences the wake of the hub and engine exhaust canopy, which affect the considered sensors. The comparison of CH results with experimental data is satisfactory, although the numerical results show higher localized pressure peaks and a higher frequency content, as confirmed by Fourier analysis in figure 8. The wake above the tail boom is also detected by the PIV measurements of the velocity modulus shown in figure 10, which refers to PIV1 planes (see the location in figure 9) at different distances from the rotor hub, from 970 to 1660 mm. The top frame refer to the IF calculations, while the other frames depict the CH calculations at different azimuthal angles. A general asymmetric wake behavior is present for both configurations, due to the asymmetry of the tail geometry and to the fact that the IF calculations feature a rotating hub. The CH results show however a more diffused wake, which extends also towards the suction side of the vertical tail.

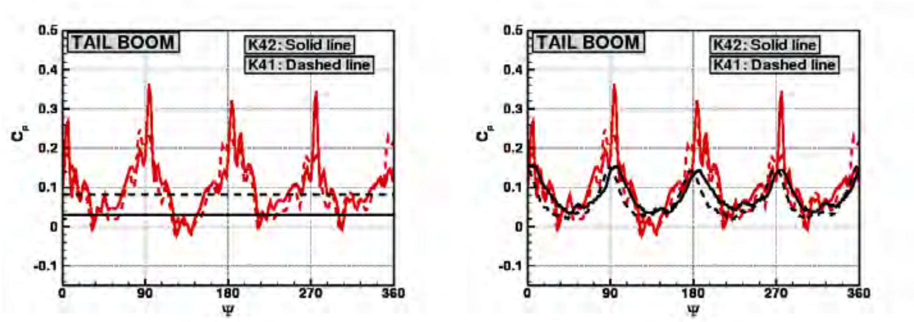

(a) Isol. Fuselage (black) vs Helicopter (red) (b) Comparison with experiments (black)

Figure 7: Effect of main rotor on fuselage pressure sensors K41-K42

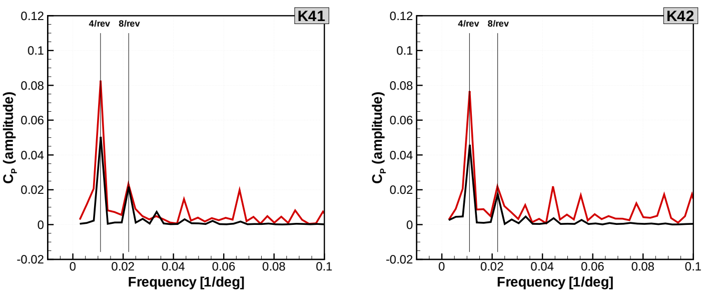

(a) K41 (b) K42

Figure 8: FFT of pressure signal for sensors K41-K42: experiments (black) and computations (red)

Figure 11 refers to the pressure sensors located at the vertical tail plane. Sensor K58 is positioned on the right side of the tail plane, where the tail rotor is present, while sensor K57 is on the opposite side. Two observations can be made here: the vertical tail is invested by a very complex flow due to the main rotor wake, the tail rotor wake and the hub wake; this combined wake appears to be fully turbulent, especially on the pressure side (K58) where both the CH computed and experimental pressure values are oscillating almost randomly. The Fourier analysis of the K58 signal allow to clearly detect the 10/rev frequency of the tail rotor, together with higher frequency contents. On the suction side (K57) is present a more pronounced 4/rev contribution, although the numerical CH results show high frequency oscillations of larger amplitude than the experimental measurements. The effect of

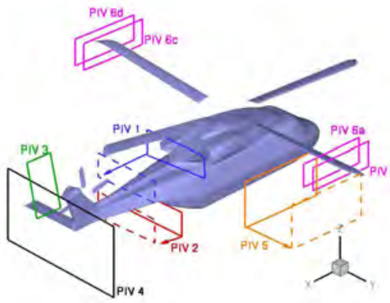

Figure 9: Location of the PIV measurement planes

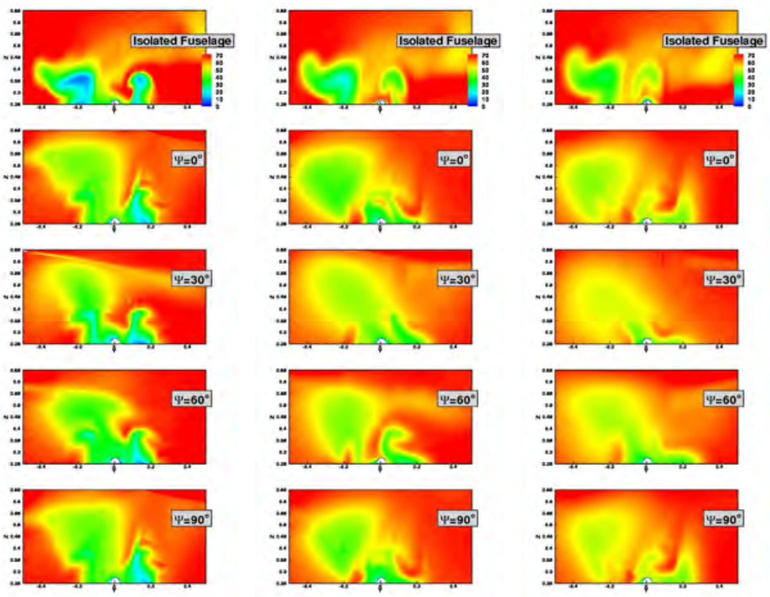

(a) x = 970 (b) x = 1320 (c) x = 1660

Figure 10: Distribution of velocity modulus above the tail boom

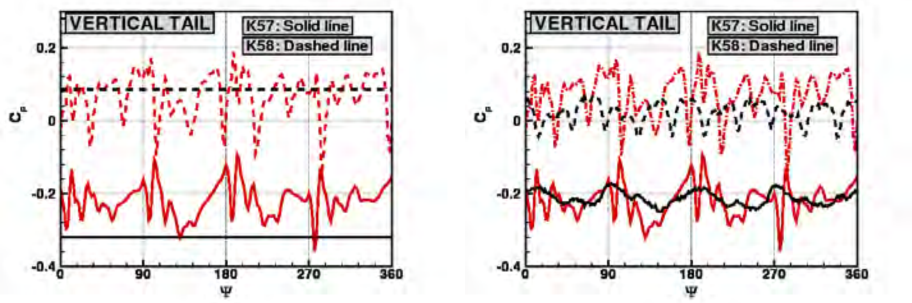

(a) Isol. Fuselage (black) vs Helicopter (red) (b) Comparison with experiments (black)

Figure 11: Effect of main/tail rotors on fuselage pressure sensors K57-K58

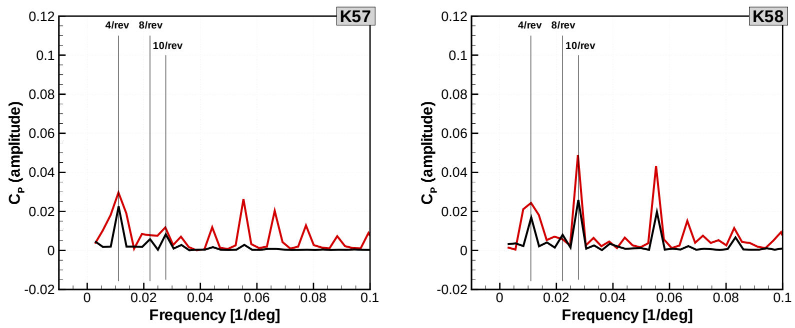

(a) K57

(b) K58

Figure 12: FFT of pressure signal for sensors K57-K58: experiments (black) and computations (red)

the main rotor wake is to slightly modify the average angle of attack of the vertical tail, as can be deduced by the comparison between the IF calculations and the averaged values of the CH results. A large variation of the mean angle of attack experimented by the horizontal stabilizer, due to the main rotor wake, is also seen in figure 13, were the chordwise pressure distribution at section V3 (see figure 4) is depicted. For the CH configuration, the averaged values are reported. It is evident that the presence of rotor wake results in a marked increase of the angle of attack of the stabilizer. Note that the correlation with experimental data is excellent for both IF and CH calculations.

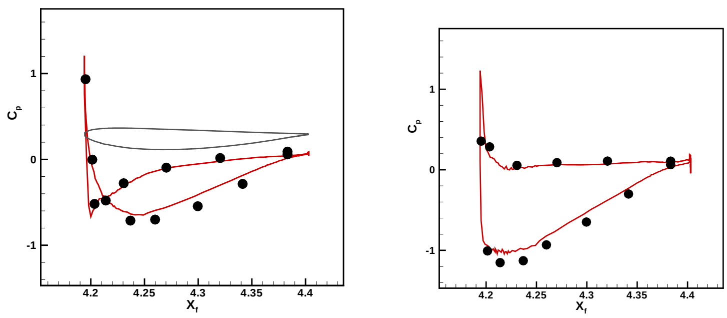

(a) Isolated Fuselage

(b) Complete Helicopter

Figure 13: Effect of main rotor on horizontal tail plane (section V3)

4.2 Fuselage on rotor interactions

The CH and IR configurations are considered to evaluate the influence exerted by the fuselage on the rotor aerodynamic loads. We focus the attention on the force coefficient $C_Z M^2$ in the direction parallel to the rotation axis, whose distribution is shown in figure 14(a) and 14(b), respectively, for the full helicopter and for the isolated rotor. A visual comparison of the two distributions is sufficient to argue that the presence of the fuselage is felt markedly by the rotor blade only for azimuth positions close to 0° and 180°, as the intuition would also suggest. This consideration is even more evident after inspection of figure 14(c), where the difference of the coefficient $C_Z M^2$ computed for the two configurations is plotted. The same picture suggests that the fuselage induces an upwash in the front part of the rotor disk (*i.e.* close to Ψ=180°) and a downwash in the rear part (across Ψ=0°). Therefore the effect of the fuselage on the rotor may be viewed as a modification of the local angle of attack of the blades.

For the considered configuration, the stronger effect is the upwash in the front part of the disk, most probably because in that region of the rotor disk the blade reaches the position closest to the fuselage. Moreover, the upwash is roughly symmetrical with respect to the fuselage centerline, while this is not true for the downwash in the rear part of the disk, where the induction effect take its maximum slightly before the blade reaches the centerline. By further inspection of figure 14(c), it can be also noted that the blade sections where most marked is the local variation of the force coefficient are those in the range $r/R = 0.3 - 0.7$. Nevertheless, in the rear part of the disk and for $r/R < 0.3$ there are also other downwash peaks, which are reasonably due to the perturbation introduced by the rotor hub.

The above considerations are also confirmed by the analysis of the pressure coefficient distribution on the blade sections at $r/R = 0.5$ and $r/R = 0.7$ reported in figures 15 and 16.

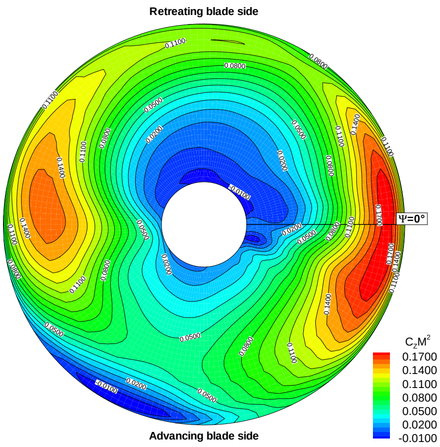

(a) Full helicopter

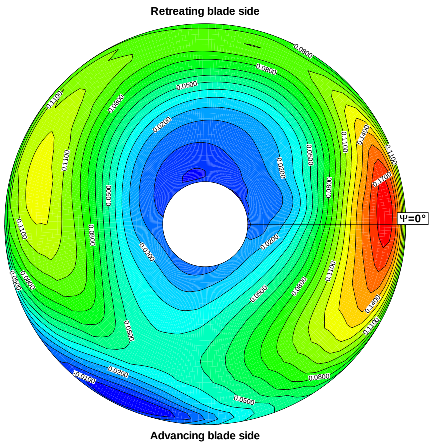

(b) Isolated rotor

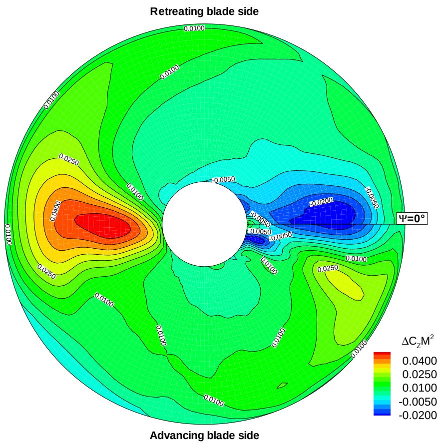

(c) Full helicopter minus isolated rotor

Figure 14: Distribution of the force coefficient $C_Z M^2$ on the rotor disk for the complete helicopter (a) and for the isolated rotor (b). Variation of $C_Z M^2$ due to the presence of the fuselage (c).

5 Conclusions

The comparison of simulations performed with the RANS solver ROSITA of an isolated rotor, an isolated fuselage and a full helicopter configuration, featuring both main and tail rotors, has allowed a preliminary analysis of the interference effects between the rotor wakes and the fixed components of the fuselage and the influence of the fuselage on the rotor loads. In parallel, the experimental data gathered from the GOAHEAD database has been compared with the computations of the full helicopter configuration. The general agreement between numerical and experimental results can be judged satisfactory, such as to validate the use of such CFD tool for aerodynamic interference studies.

For the cruise flight condition here examined, most of the interference effects deals with the influence of the wakes on the vertical and horizontal tail planes, where highly unsteady flow is observed, together with a direct or indirect influence of main and tail rotor wakes.

Acknowledgements: this work has been partially funded by the European Union under the 6th Framework Specific Targeted Research Project GOAHEAD, contract N. 516074. The Authors wish to thank Dr. W. Khier, DLR Braunschweig, for providing some of the grids used in this work.

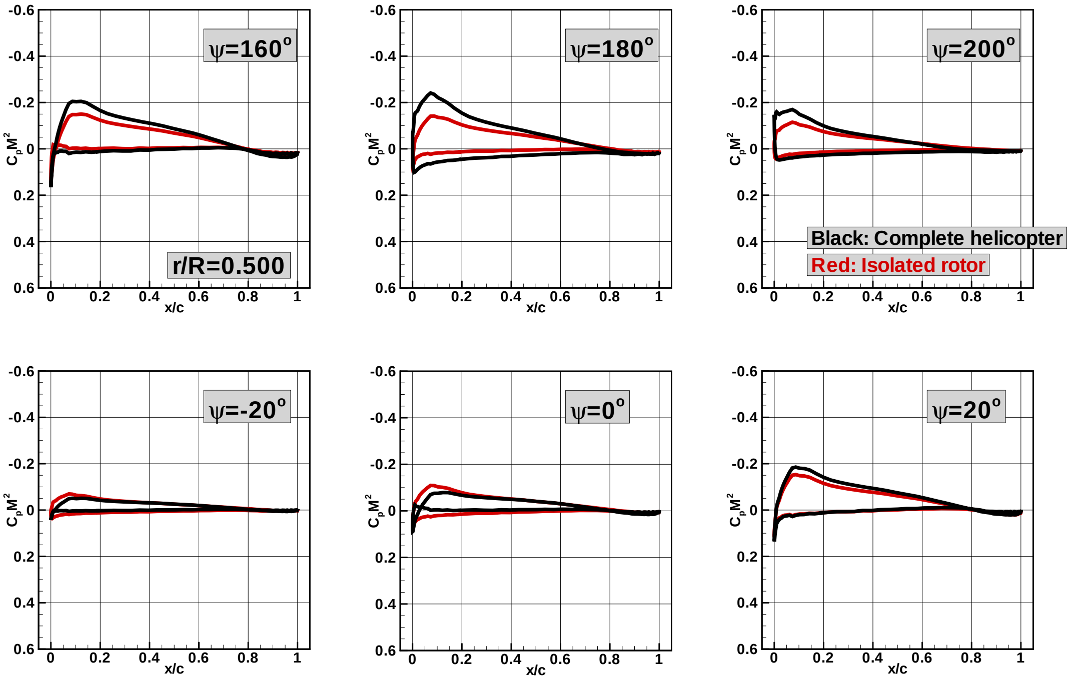

Figure 15: Distribution of the pressure coefficient $C_P M^2$ on the main rotor blade radial station $r/R = 0.5$. Full helicopter (black), isolated rotor (red).

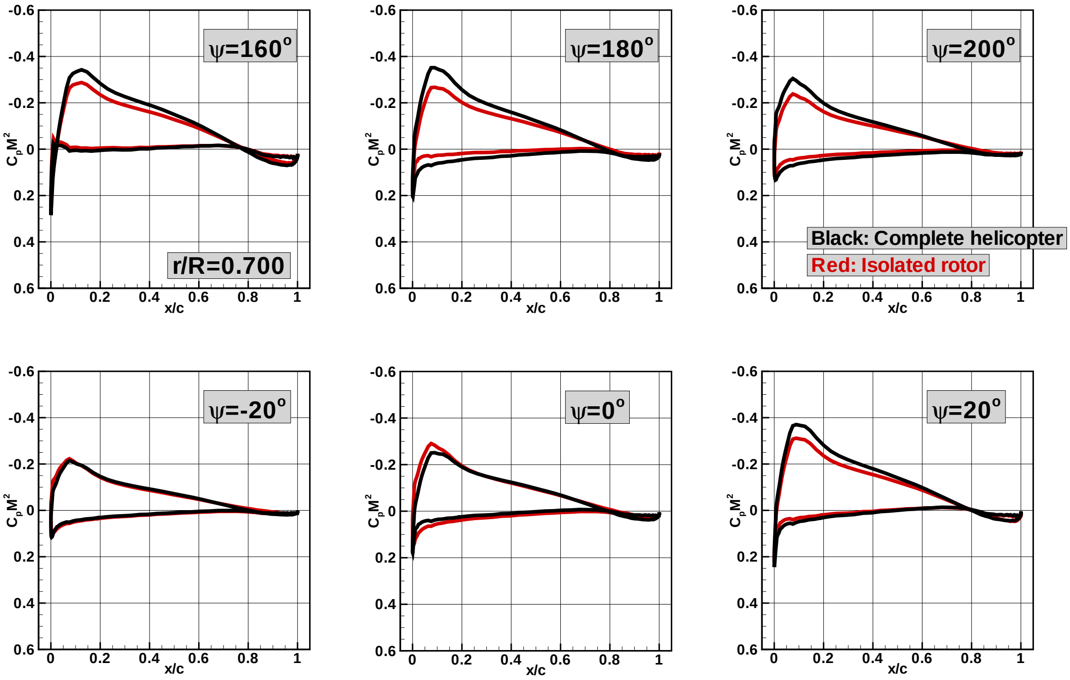

Figure 16: Distribution of the pressure coefficient $C_P M^2$ on the main rotor blade radial station $r/R = 0.7$. Full helicopter (black), isolated rotor (red).

References

[1] P.F. Sheridan and R. P. Smith. Interactional aerodynamics - a new challenge to helicopter technology. *J. Am. Helicopter Soc.*, 25:3–21, 1980.

[2] S. Liou, N. Komerath, and H. McMahon. Velocity measurements of airframe effects on a rotor in low-speed forward flight. *AIAA J.*, 26:340–348, 1989.

[3] J. Kim and N. Komerath. Summary of the interaction of a rotor wake with a circuar cylinder. *AIAA J.*, 33:470–478, 1995.

[4] J. G. Leishmann and N. Bi. Measurements of a rotor flowfield and the effects on a fuselage in forward flight. *Vertica*, 14:401–415, 1990.

[5] J. G. Leishmann and N. Bi. Aerodynamic interactions between a rotor and a fuselage in forward flight. *J. Am. Helicopter Soc.*, 35:22–31, 1990.

[6] C. Freeman and R. Mineck. Fuselage surface pressure measurements of a helicopter wind-tunnel model with a 3.15-meter diameter single rotor. Technical report, NASA TM-80051, 1979.

[7] R. Mineck and S. Althoff. Steady and periodic pressure measurements on a generic helicopter fuselage model in the presence of a rotor. Technical report, NASA TM-2000-210286, 2000.

[8] G. L. Crouse, J. G. Leishmann, and N. Bi. Theoretical and experimental study of unsteady rotor/body aerodynamic interactions. *J. Am. Helicopter Soc.*, 37:55–65, 1992.

[9] R. Steijl and G. Barakos. Computational study of helicopter rotor-fuselage aerodynamic interactions. *AIAA J.*, 47:2143–2157, 2009.

[10] T. Renaud, C. Benoit, J.-C. Boniface, and P. Gardarein. Navier–Stokes computations of a complete helicopter configuration accounting for main and tail rotor effects. In *29th European Rotorcraft Forum, Friedrichshafen, Germany*, 2003.

[11] W. Khier, T. Schwarz, and J. Raddatz. Time accurate simulation of the flow around the complete BO105 wind tunnel model. In *31st European Rotorcraft Forum, Florence, Italy*, 2005.

[12] W. Khier, M. Dietz, T. Schwarz, and S. Wagner. Trimmed CFD simulation of a complete helicopter configuration. In *33rd European Rotorcraft Forum, Kazan, Russia*, 2007.

[13] M. Dietz, W. Khier, S. Wagner, and E. Krämer. Numerical simulation of a full helicopter configuration using weak fluid-structure coupling. In *46th AIAA Aerospace Science Meeting and Exhibit, Reno, Nevada. AIAA 2008-401*, 2008.

[14] M. Raffel, F. de Gregorio, W. Sheng, G. Gibertini, A. Seraudie, K. de Groot, and B. van der Wall. Generation of an advanced helicopter experimental aerodynamic database - the wind tunnel test of the EU-Project GOAHEAD. In *35th European Rotorcraft Forum, Hamburg, Germany*, 2009.

[15] O. Boelens, G. Barakos, M. Biava, A. Brocklehurst, M. Costes, A. D'Alascio, M. Dietz, D. Drikakis, J. Ekaterinaris, I. Humby, W. Khier, B. Knutzen, F. Le Chiuton, K. Pahlke, T. Renaud, T. Schwarz, R. Steijl, L. Sudre, L. Vigevano, and B. Zhong. The blind-test activity of the GOAHEAD project. In *33rd European Rotorcraft Forum, Kazan, Russia*, 2007.

[16] W. Khier. Numerical simulation of air flow past a full helicopter configuration. In *35th European Rotorcraft Forum, Hamburg, Germany*, 2009.

[17] M. Biava, J.-C. Boniface, and L. Vigevano. Influence of wind-tunnel walls in helicopter aerodynamics predictions. In *31st European Rotorcraft Forum, Firenze, Italy*, 2005.

[18] M. Biava. *RANS computation of rotor/fuselage unsteady interactional aerodynamics*. PhD thesis, Politecnico di Milano, 2007.

[19] M. Biava, A. Pisoni, A. Saporiti, and L. Vigevano. Efficient rotor aerodynamics predictions with an Euler method. In *29th European Rotorcraft Forum, Friedrichshafen, Germany*, 2003.

[20] V. Venkatakrishnan. On the accuracy of limiters and convergence to steady state solutions. In *31st AIAA Aerospace Science Meeting and Exhibit, Reno, Nevada. AIAA 1993-880*, 1993.

[21] G. Chesshire and W. D. Henshaw. Composite overlapping meshes for the solution of partial differential equations. *J.Comput. Phys*, 90:1–64, 1990.

[22] W. M. Chan and P. G. Buning. Zipper grids for force and moment computation on overset grids. In *12th AIAA Computational Fluid Dynamics Conference, San Diego, CA. AIAA 1995-1681*, 1995.